Defect Engineering and Phase Junction Architecture of Wide-Bandgap ZnS for Conflicting Visible Light Activity in Photocatalytic H₂ Evolution

Zhibin Fang, Sunxian Weng, Xinxin Ye, Wenhui Feng, Zuyang Zheng, Meiliang Lu, Sen Lin,* Xianzhi Fu,* and Ping Liu*

Research Institute of Photocatalysis, State Key Laboratory of Photocatalysis on Energy and Environment, College of Chemistry, Fuzhou University, Fuzhou 350002, P. R. China

Ⓢ Supporting Information

ABSTRACT: ZnS is among the superior photocatalysts for H₂ evolution, whereas the wide bandgap restricts its performance to only UV region. Herein, defect engineering and phase junction architecture from a controllable phase transformation enable ZnS to achieve the conflicting visible-light-driven activities for H₂ evolution. On the basis of first-principle density functional theory calculations, electron spin resonance and photoluminescence results, etc., it is initially proposed that the regulated sulfur vacancies in wurtzite phase of ZnS play the key role of photosensitization units for charge generation in visible light and active sites for effective electron utilization. The symbiotic sphalerite-wurtzite phase junctions that dominate the charge-transfer kinetics for photoexciton separation are the indispensable configuration in the present systems. Neither ZnS samples without phase junction nor those without enough sulfur vacancies conduct visible-light photocatalytic H₂ evolution, while the one with optimized phase junctions and maximum sulfur vacancies shows considerable photocatalytic activity. This work will not only contribute to the realization of visible light photocatalysis for wide-bandgap semiconductors but also broaden the vision on the design of highly efficient transition metal sulfide photocatalysts.

KEYWORDS: sulfur vacancy, phase junction, visible light photocatalysis, ZnS, first principle DFT
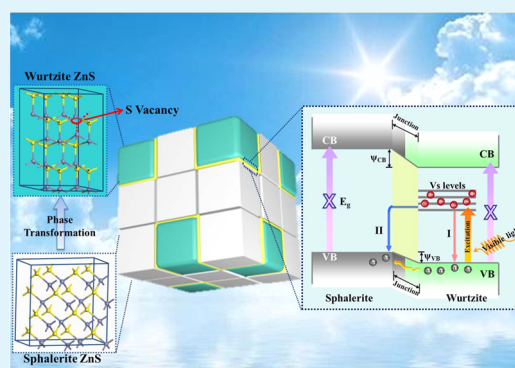
■ INTRODUCTION

Hydrogen is an ideal fuel with excellent energy capacities and clean combustion products. Photocatalytic water splitting, which converts the inexhaustible solar energy into hydrogen, is one of the most promising and hot techniques to address the severe situations of global energy and environmental issues. In this field, the development of highly efficient photocatalyst systems has always been pursued by researchers.[1−3] Highly efficient photocatalysts generally possess characteristics including wide response in the sunlight spectrum (ultraviolet, visible, and even near-infrared region) to generate charges, constructions to facilitate charge separation, and abundant active sites to utilize charge carriers in proper photocatalytic reactions. ZnS, an important II−VI group transition metal sulfide, is well-known for its high theoretical efficiency of photocarrier generation, which is much higher than the most famous photocatalyst TiO₂.[4] Moreover, owing to its relatively negative potential of conduction band, the photoinduced electrons of ZnS possess impressive abilities to reduce protons to H₂ even in the absence of noble metal cocatalysts like Pt.[5,6] Unfortunately, the pristine ZnS only responds to UV light (∼5% of the solar spectrum) due to its wide band gap (3.6−3.8 eV), one of the main restrictions on its applications. Thus,

shifting its light response for visible light photocatalysis is among the urgent issues toward a bright prospect of highly efficient ZnS photocatalyst.

As a common sense, the nature of materials determines their mechanisms and performances in reactions, including photocatalytic hydrogen evolution reactions (HER). For instance, defect states,[7−11] crystalline phases,[12,13] exposed facets,[14−16] etc., of semiconductor photocatalysts can regulate the light response for robust charge generation, dominate the kinetics of charge transfer for effective charge separation, and organize active sites or facets for resultful charge utilization. All these three aspects of charge behaviors constitute the crucial factors of superior photocatalysis activities. Therefore, it is of significance and potential by investigating the intrinsic properties and schemes of ZnS to approach its visible light photocatalysis. However, compared with the rich efforts in introducing extrinsic elements (Cu, Ni, Cd, In, ...) or organic/inorganic components to ZnS,[17−27] the intrinsic modifications

without extrinsic element introduction for the visible light photocatalysis of ZnS are rarely reported.

Differing in the stacking sequence of Zn and S atom layers, ZnS is divided in two major crystalline phases: cubic sphalerite and the hexagonal wurtzite, with different properties.[19] The sphalerite ZnS can transform into the wurtzite ZnS when undergoing either high-temperature annealing processes[28,29] or solvent-assisted thermal treatments.[30,31] As a process of atom rearrangement, the phase transformation inevitably generates crystal defects including sulfur vacancies.[32,33] The diverse defect states from the crystal growth make ZnS competent to vary in its optical and excitonic properties.[34−37] Our density functional theory (DFT) calculation results demonstrate that sulfur vacancies can narrow the band gap of ZnS by forming defect energy levels in the band gap (provided hereinafter). This suggests an opportunity to facilitate ZnS to absorb visible light. In other words, the visible-light-driven charge generation of ZnS may be feasible by engineering of the sulfur vacancies. Meanwhile, the sphalerite-to-wurtzite phase transformation can form phase junctions, an advantageous architecture reported in TiO_2 systems,[12] Ga_2O_3 systems,[13] and Bi_2O_3 systems.[38] Thereby, the facilities for the separation of the photoinduced electron−hole pairs can be simultaneously constructed.

On the basis of the above analysis, in this work, sulfur vacancy engineering and phase junction architecture on ZnS are accomplished by controlling the extent of sphalerite-to-wurtzite phase transformation. Combining theory calculations and experimental results, we initially proposed the dual function of sulfur vacancies, which sensitize ZnS for visible light response and trap photoinduced electrons for utilization in H_2 evolution. The coexisting sphalerite-wurtzite phase junctions drive the transfer kinetics of charge carriers leading to effective separation. The synergy between sulfur vacancies and phase junctions enable wide-bandgap ZnS to perform desirable photocatalytic activities for H_2 evolution under visible light irradiation.

■ EXPERIMENTAL SECTION

Synthesis. ZnS samples with different sphalerite-wurtzite ratios were fabricated via modified hydrothermal processes with the $ZnS(EN)_{0.5}$ (EN = ethylenediamine) precursor.[30,39] The $ZnS(EN)_{0.5}$ is prepared by a solvothermal reaction of Zn^{2+} with thiourea in ethylenediamine medium at 160 °C.[21,30] Then the ZnS samples were obtained after hydrothermal decomposition of the $ZnS(EN)_{0.5}$ precursor in 140, 180, 200, and 230 °C for 12 h, labeled as ZS-140, ZS-180, ZS-200, and ZS-230, respectively. To obtain high-percentage and pure hexagonal wurtzite ZnS, ethanol and carbon disulfide were used as solvents instead of water, while the temperatures of the solvothermal reaction were 200 and 180 °C for 12 h, respectively (labeled as w-ZS-E and w-ZS-CS2, respectively). Pure cubic sphalerite ZnS (denoted as C-ZS) was synthesized via hydrothermal reaction between purchased cubic ZnO and excess thioacetamide at 200 °C for 24 h. Details are present in Supporting Information.

Characterization. Crystal structure identification was performed using Bruker D8 X-ray diffractometer (XRD) with Cu Kα radiation (λ = 0.154 18 nm) operating at 40 kV and 40 mA. Morphologies of the samples were measured by a field-emission scanning electron microscope (SEM; FEI NovaNanoSEM-230). Microstructures were investigated using transmission electron microscopy (TEM) measured on a TecnaiG2F20 S-TWIN (FEI company) with a field emission gun at 200 kV. Nitrogen adsorption and desorption isotherms were recorded on a Micrometrics ASAP 2020 analyzer. During the degassing process, the samples were held at 140 °C for 3 h. The optical absorption properties of the samples were analyzed using the ultraviolet−visible diffuse reflectance spectroscopy (UV−vis DRS)

with a UV−vis spectrophotometer (Lambda 950, PerkinElmer Co.) in which $BaSO_4$ acted as the background. X-ray photoelectron spectroscopy (XPS) analysis was conducted on an ESCALAB 250 photoelectron spectroscope (Thermo Fisher Scientific) at 1.2×10^{-9} mbar using an Al Kα X-ray beam (1486.6 eV). The XPS spectra were charge-corrected to the adventitious C 1s peak at 284.6 eV. A Bruker model A300 spectrometer was used to investigate the electron spin resonance (ESR) signals of samples. The settings of ESR were as follows: microwave power, 6.35 mW; frequency, 9.86 GHz; center field, 3512.48 G. The photoluminescence (PL) spectra were obtained using an Edinburgh Analytical Instrument FL/FSTCSPC920 Spectrophotometer.

The electrochemical impedance spectra (EIS) test was conducted using a ZENNIUM electrochemical workstation (Zahner, Germany) with a conventional three-electrode system. The reference and counter electrodes were Ag/AgCl and Pt plates, respectively, and 0.2 M Na_2SO_4 (pH = 6.8) aqueous solution served as the electrolyte. Different ZnS samples dispersed in N,N-dimethylformamide (DMF) solution were evenly spread onto indium tin oxide glass substrates and served as the working electrode. The flat-band potential (V_{fb}) of the semiconductor space charge region was evaluated by the Mott−Schottky plot.

Density Functional Theory Calculations. All DFT calculations were performed using the Vienna ab initio simulation package (VASP)[40−42] with the gradient-corrected PW91 exchange-correction functional.[43] The ionic cores were described with the projector augmented-wave (PAW) method,[44] and for valence electrons a plane-wave basis set[45] with an energy cutoff of 550 eV was employed. The Brillouin zone was sampled using a $2 \times 2 \times 1$ Monkhorst−Pack k-point grid,[46] which was tested to be converged. Unit cells ($2 \times 2 \times 2$ and $2 \times 1 \times 2$) were employed for sphalerite and wurtzite ZnS, respectively, with all atoms relaxed.

Photocatalytic Activity Test. The photocatalytic H_2 evolution experiments were conducted in a top-irradiation vessel connected to a glass-enclosed gas circulation system. In a typical run, 50 mg of sample was suspended in 100 mL of 5% lactic acid aqueous solution under magnetic stirring. After the system was degassed for 1 h, a 300 W Xe lamp with a 410 nm cutoff filter was applied to execute the photocatalytic reaction. The products were analyzed using a gas chromatograph (TECHCOMP GC7900) equipped with a thermal conductivity detector (TCD).

■ RESULTS AND DISCUSSION

Formation and Function of Sphalerite−Wurtzite Phase Junctions. According to the previous report from Zhou et al.,[30] water medium leads to mixed-phase ZnS in the thermal condition. Hydrothermal treatment is thereby employed to confirm the feasibility to control the phase transformation process from sphalerite to wurtzite by ranging the reaction temperature. The results are demonstrated by X-ray diffraction patterns. As is shown in Figure 1, diffraction peaks of the ZS-140 sample are well-indexed to cubic sphalerite ZnS (JCPDS No. 03−065−0309), while weak diffraction peaks at 27.0° and 30.5° belonging to the hexagonal wurtzite phase are also detected, indicating the phase transformation has been in progress under hydrothermal condition at 140 °C. As the hydrothermal temperature rises from 140 to 230 °C, the intensities of the characteristic peaks for wurtzite ZnS located at 27.0°, 30.5°, 39.6°, and 51.8° increase gradually. The intensity ratio of the peaks at 27.0° and 28.6° ($I_{27.0}/I_{28.6}$), which declares the mounting percentage of the wurtzite phase in the overall crystals, rises with the hydrothermal temperature (Table S1 in Supporting Information), indicating a temperature-dependent phase transformation for ZnS in the hydrothermal condition. From the XRD results we can see that the phase transformation from sphalerite to wurtzite depends on the hydrothermal temperature; that is, the control can be achieved by adjusting
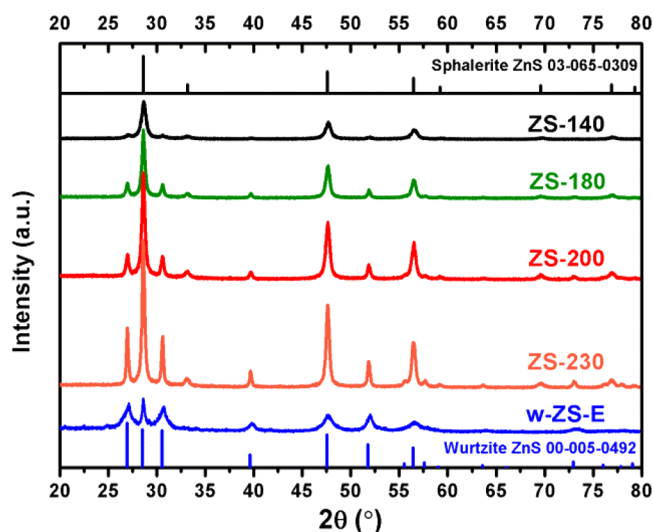
Figure 1. XRD patterns of as-prepared samples.

Figure 2. (a) TEM image and (b) SAED patterns of the ZS-200 sample; (insets) the atom configurations of cubic sphalerite (upper) and hexagonal wurtzite (lower). (c, d) HRTEM images of the ZS-200 sample.

the reaction temperature. Besides, w-ZS-E sample with high-percentage wurtzite was synthesized using ethanol instead of water as the solvent since all of the peaks of the w-ZS-E sample are indexed to wurtzite ZnS (JCPDS No. 00−005−0492). Compared to the pattern of JCPS No. 00005−0492, the diffraction peak at 28.6° overtops that at 27.0° for w-ZS-E sample, implying trace amount of sphalerite phase probably exists in the sample. This is further discussed upon the following ESR experiments. Pure wurtzite ZnS with well-matched XRD peaks is obtained using CS_2 as the solvent in solvothermal reaction (Supporting Information, Figure S1).

As two crystalline phases coexist in a sample, it can be inferred that sphalerite−wurtzite (S−W) phase junctions, considered as the transitional structures in the process, may form at the interface between sphalerite and wurtzite crystalline phase. Thus, the crystalline microstructure of ZS-200 sample with a medium S−W ratio was investigated by the transmission electron microscopy (TEM). The selected area electron diffraction (SAED) pattern in Figure 2b corresponds to the nanoparticles in Figure 2a. Since ZS-200 consists of both crystal phases, there are two sets of diffraction spots in Figure 2b, coinciding with the atom configurations of cubic sphalerite (inset, upper right) and hexagonal wurtzite (insert, lower right), respectively. Considerable stacking faults (SF, circled in yellow dash line in Figure 2a) are found in the nanoparticles, and twins (T) are observed in high-resolution TEM visions as is shown in Figure 2c.[47,48] According to the previous reports, the phase transformation of ZnS is most likely to start and develop from these imperfect sites.[48] And as the hexagonal wurtzite structure circulates, the interface between sphalerite and wurtzite grows, resulting in the formation of in situ phase junctions. As shown in Figure 2d, the gradually changing lattice fringes located between wurtzite and sphalerite demonstrate the obtained S−W phase junctions. The S−W phase junction structures also exist in ZS-180 and ZS-230, as shown in Supporting Information, Figure S2d,f clearly. Furthermore, considering the ranging extent of the phase transformation, the quantity of the phase junctions is believed to differ in each ZnS sample and reach an extremum at a balanced S−W proportion.

It has been demonstrated that the junctions formed between two crystal phases with different energy band structures in one semiconductor photocatalyst can be favorable for the separation
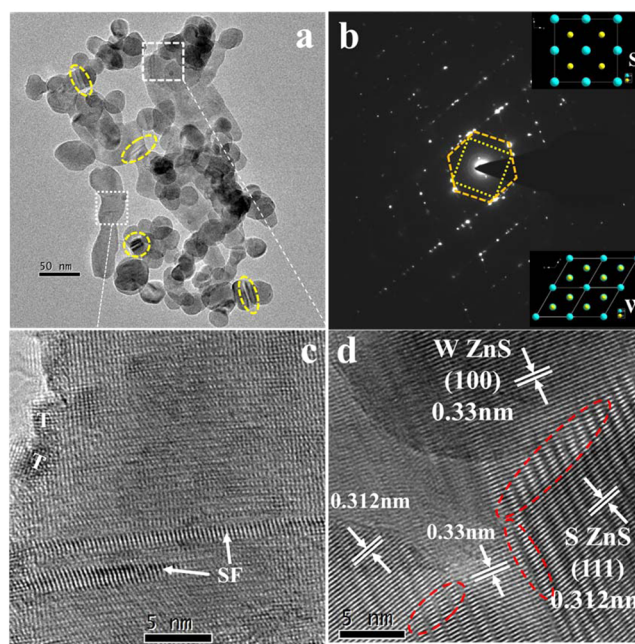
of the photoinduced charge carriers.[12,13,38] In this case, the energy band structures of sphalerite and wurtzite ZnS should be surveyed. As ZS-140 and w-ZS-E samples are in approximately pure crystal phases of sphalerite ZnS and wurtzite ZnS, respectively, the measurements for the energy band structures are conducted using these two samples. The measured XPS valence band (VB) potentials of ZS-140 and w-ZS-E are 1.36 and 1.59 eV, respectively (Figure 3a); that is, the sphalerite ZnS possesses a more positive VB than the wurtzite ZnS. The difference in the conduction-band potentials for the two phases can be revealed by measuring the flat-band potentials of ZS-140 and w-ZS-E, which are considered to be located just under the conduction band (CB) for semiconductors. As is shown in the Mott−Schottky curves (Figure 3b), the flat-band potentials are −1.30 and −1.06 eV versus Ag/AgCl electrodes for ZS-140 and w-ZS-E, respectively. Then the CB of the sphalerite ZnS is more negative than that of the wurtzite ZnS. Thus, a band structure similar to the type II heterojunction[49] can be formed in ZnS samples with S−W phase junctions. Once ZnS is intrinsically activated by the photon energy to generate electron−hole pairs, electrons in the CB of sphalerite phase drift into that of wurtzite phase, while holes in the VB of wurtzite phase will be driven to that of sphalerite phase in the type II junctions. Then charge carriers are effectively separated. The electrochemical impedance spectra (EIS) tests show that ZS-200 possesses a smaller arc radius of Nyquist plots than ZS-140 and w-ZS-E (Supporting Information, Figure S3), suggesting a weaker charge-transfer resistance,[50] that is, a higher transfer rate. That means a better charge separation is approached[51] in ZS-200, which contains more phase junctions, revealing the positive function of the junctions.

Generation of Sulfur Vacancies. In general, the S−W phase transformation originates from the atomic displacement in the sphalerite (ABCABC··· stacking series) to wurtzite (ABABAB··· stacking series), driven by thermal energy.[48] The rearrangement of ZnS atom pair opportunistically leaves some
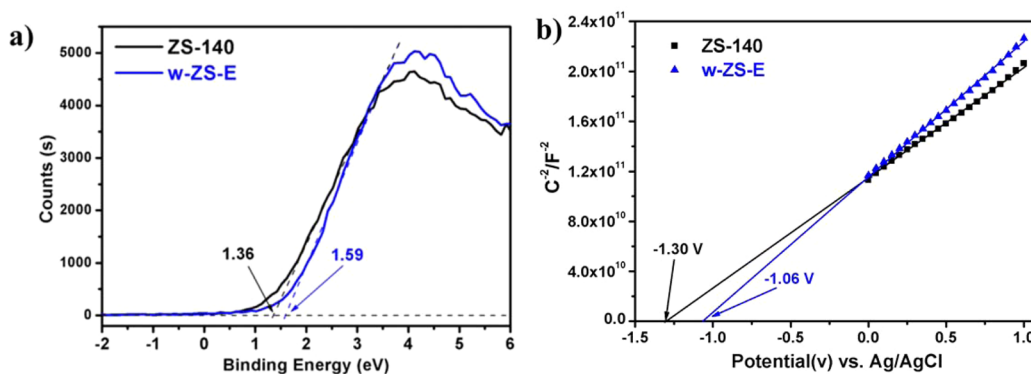
Figure 3. (a) XPS valence band spectra of ZS-140 and w-ZS-E; (b) Mott–Schottky curves of ZS-140 and w-ZS-E electrodes.
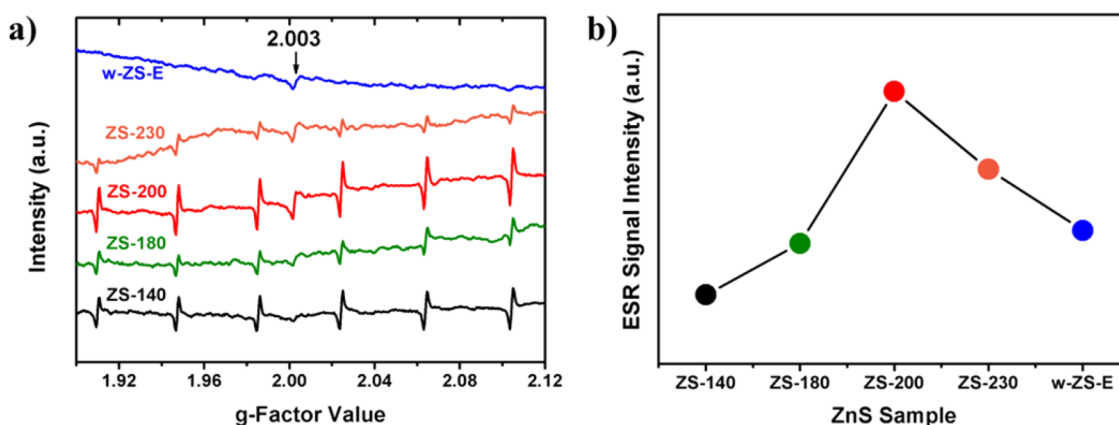

Figure 4. (a) Room-temperature ESR spectra of the as-prepared ZnS samples. (b) Calculated intensities of ESR signal at g = 2.003 for the as-prepared ZnS samples.

delocalized atoms and dangling bonds behind ascribed to the crystalline mismatch of the two phases with different lattice constants, giving rise to crystal defects. To verify the formation of defects and identify the defect species during the phase transformation, the electron spin resonance (ESR) spectroscopy was employed, as displayed in Figure 4. Six hyperfine lines with g-factor value located at 1.910, 1.947, 1.985, 2.024, 2.064, and 2.104, respectively, are easily observed at room temperature in samples containing apparent sphalerite phase, that is, ZS-140, ZS-180, ZS-200, and ZS-230 (Figure 4a). These lines were commonly observed and discussed in Mn^{2+}-doped ZnS systems, which may originate from the crystal field of cubic ZnS.[52,53] To further figure out the attribution of the six hyperfine lines, ESR measurements were also conducted on the pure cubic sphalerite ZnS sample (C-ZS; see XRD patterns in Supporting Information, Figure S1) and six symmetric intensive hyperfine lines with the same g value were obtained (Supporting Information, Figure S4). Thus, it is reasonable to index the six ESR hyperfine lines to cubic sphalerite ZnS phase. Besides, the w-ZS-E sample shows six extremely weak lines at the same g values, suggesting trace amount of sphalerite phase is retained. That is consistent with the XRD results.

Note that a signal located at g = 2.003 was detected with varied intensities in the as-prepared mixed-phase samples. Summarized from previous reports on EPR studies of ZnS, this signal was assigned to the F center, a singly negatively charged sulfur vacancy,[54−58] confirming the existence of sulfur vacancies. On the contrary, no signal of sulfur vacancies was detected in C-ZS (Supporting Information, Figure S4), the pure sphalerite ZnS without the experience of phase trans-

formation. These two results suggest that the formation of sulfur vacancies is due to the phase-transformation process, consistent with the previous analysis. And for the reason that the S−W phase junctions are located in the phase interfaces where the transformation proceeds, the initially induced sulfur vacancies should stand close to the S−W phase junctions. Since the ESR signal intensity is related to the density of the defects,[57,59,60] we measured the intensity of the signal at g = 2.003 to estimate the density of sulfur vacancies for each sample and subsequently obtained a tendency displayed in Figure 4b. To understand the reason for the density differences among these samples prepared in different temperatures, we must consider the origin of sulfur vacancies, that is, the S−W phase transformation process. As proved by XRD results, the hydrothermal temperature determines the extent of phase transformation for ZnS within the same period of reaction time. In low temperatures (i.e., 140 °C), sphalerite phase starts atomic rearrangement at the imperfect sites of the crystalline slowly, and only small quantity of wurtzite grows, resulting in trace amount of sulfur vacancies in the nascent wurtzite phase; when in higher temperatures (i.e., 180 °C), the phase transformation proceeds easier and faster so that more wurtzite phase develops across the ZnS nanoparticle. Thus, the amount of sulfur vacancies increases; as the temperature further rises, besides the improved development of wurtzite phase the crystal perfection that decrease sulfur vacancies and S−W interfaces must be taken into account. Thereby, both sulfur vacancies and the S−W junction will reach top amounts or percentages at medium temperatures (i.e., 200 °C) and then decrease at higher temperatures (i.e., 230 °C) as the crystal perfection fills

the sulfur vacancies through further atomic perturbation and reduces S−W junctions when neighbor ZnS nanoparticles in a region transfer into wurtzite totally. Finally, all the nanoparticles will become pure wurtzite with some residual sulfur vacancies in the bulk. Since the phase transformation of the ZnS precursor can be promoted in ethanol solvents compared with water,[30] w-ZS-E approximately accomplish the transformation process at 200 °C, while the relative low temperature is not enough to drive the elimination of all sulfur vacancies. Thus, the above temperature-dependent transformation brings about a variation of sulfur vacancy amount, which is demonstrated by the intensity tendency of ESR signals in Figure 4b.

Dual Roles of Sulfur Vacancies in ZnS. To understand the effect of the introduced sulfur vacancies on the electronic structures of ZnS, DFT calculations are performed by using ZnS with and without sulfur vacancies as the models. Figure 5a,c shows the calculated energy band structures of perfect
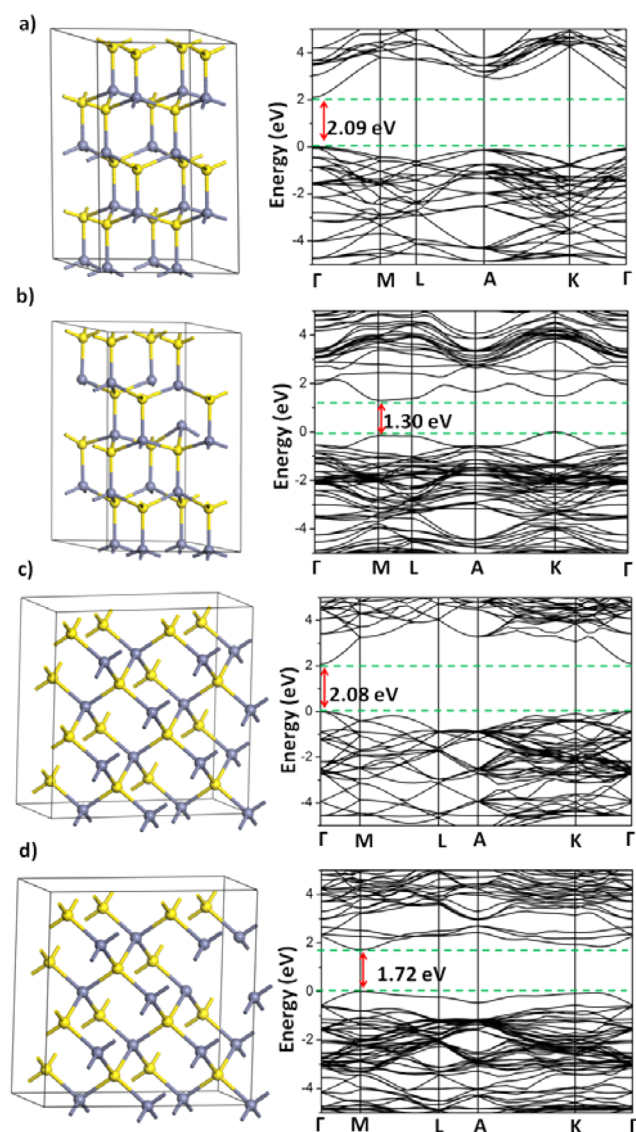

Figure 5. Calculated geometry configurations (left) and electronic band structures (right) for the crystal cells of (a) perfect wurtzite ZnS; (b) wurtzite ZnS with S vacancy; (c) perfect sphalerite ZnS, and (d) sphalerite ZnS with S vacancy; color scheme: Zn (blue), S (yellow).

wurtzite ZnS and sphalerite ZnS with band gaps of 2.09 and 2.08 eV, respectively, which are smaller than the reported experimental values (3.6 to ~3.8 eV) as a result of the well-known band gap underestimation of standard DFT.[61] When an S vacancy is introduced in the crystal cells, new energy levels form above the valence-band maximum (VBM) and below the conduction-band minimum (CBM; Figure 5b,d). As a consequence, the band gaps of wurtzite ZnS and sphalerite ZnS are reduced to 1.30 and 1.72 eV, respectively, indicating that the sulfur vacancies-involved ZnS might be a potential visible-light-responsive photocatalyst. In addition, since defective wurtzite ZnS possesses a much smaller bandgap than defective sphalerite ZnS, it can be predicted that the more sulfur vacancies-involved wurtzite phase forms, the more likely it is to broaden visible light response region of ZnS. As shown in Figure 6a, w-ZS-E sample, approximately pure wurtzite with sulfur vacancies, shows the most intensive tail absorption among the samples. The presence of this tail absorption may reflect the existence of defects, which leads to the formation of localized states extended in the bandgap,[62] in agreement with our deduction from DFT calculation results. The light response of ZS-200 is intense over ZS-230, consistent with the sulfur vacancy amount comparing from ESR results of these two samples. The reason suggested is that wurtzite phase in ZS-200 occupies more sulfur vacancies than ZS-230 though ZS-230 contains a higher percentage of wurtzite than ZS-200, inducing a more effective narrowing in the band gap. On the basis of the results of DFT calculations and DRS measurements, we have the justification to believe that the introduced sulfur vacancies in the present mixed-phase ZnS systems act as photosensitization units that endow ZnS with a visible light response.

In most cases, an appropriate amount of defects in semiconductor photocatalysts can trap the photoactivated electrons or holes leading to an improved charge separation in an advantageous way,[9] or excessive and uncontrollable defects become the recombination centers for the electrons and holes resulting in a disadvantageous way.[63,64] It is the competition between these two aspects that determine the overall effect of defects. Thus, it is worth considering the spatial behavior of sulfur vacancies to the photoactivated charge kinetics. In the case of sulfur vacancy, the absence of anion may cause the affinity to attract electrons; that is, the photoactivated electrons should be enriched in sulfur vacancies. As the present ZnS samples can respond to visible light according to the DRS results, we conducted the photoinduced ESR measurement under visible-light illumination ($\lambda \geq 410$ nm). As shown in Figure 6b, the signal at $g = 2.003$ is obviously enhanced under illumination. The enhancement suggests an increase of single electrons located at the vacancies, demonstrating the behavior to trap photoactivated electrons[24] for the sulfur vacancy. Note that, as the type II phase junctions can drive holes from VB of wurtzite phase to sphalerite phase, electrons trapped in sulfur vacancies will be significantly utilized in proton reduction. From this point of view, sulfur vacancies are serving as active sites for the photocatalytic HER.

Therefore, the dual roles of sulfur vacancies, photosensitization units for visible light response and active sites for electron utilization, are disclosed. Both of the functions are beneficial to the photocatalytic HER performances of ZnS.

Photocatalytic Performance in H$_2$ Evolution under Visible-Light Illumination. On the basis of above results and discussions, it is imperative to study the overall effect of the introduced S−W phase junctions and S vacancies on the
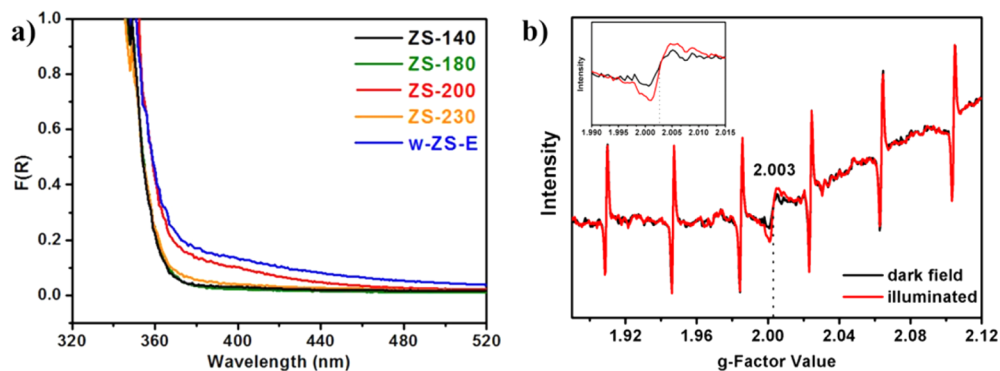
Figure 6. (a) UV−vis diffuse reflectance spectra of the as-prepared ZnS samples; (b) room-temperature ESR spectra for ZS-200 in dark field and under visible-light illumination ($\lambda \geq 410$ nm); (inset) expanded x-axis around $g = 2.003$.

photocatalytic property of ZnS for H_2 evolution under visible-light illumination ($\lambda \geq 410$ nm). As a member of wide-bandgap semiconductors (Supporting Information, Figure S5), pristine ZnS (C-ZS sample) shows no activities in visible-light region. When the S−W phase junctions and sulfur vacancies are simultaneously brought into ZnS via phase transformation, the samples indeed exhibit considerable capacities for visible-light-driven H_2 evolution (Figure 7). Among the hydrothermally
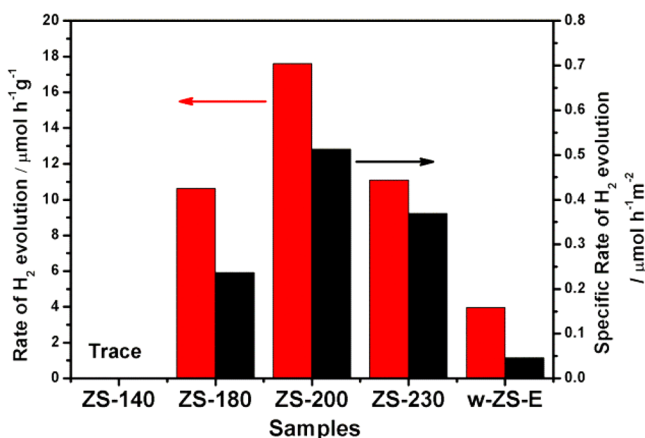

Figure 7. Photocatalytic H_2 evolution performances of the as-prepared ZnS samples under visible-light illumination ($\lambda \geq 410$ nm) in lactic acid aqueous solution.

fabricated samples, ZS-200 with balanced amount of sulfur vacancies and phase junctions from the medium-extent phase transformation shows the best activity. ZS-140 with the least extent of phase transformation exhibits poor H_2 production that cannot be detected. For w-ZS-E sample, the completing phase transformation toward pure wurtzite indicates the trace amount of phase junction, but the residual sulfur vacancies still contribute to the generation of photoexcitons under visible-light irradiation, so H_2 evolution could be proceeded in low level.

Considering other important factors that affect the activities of the photocatalysts, we analyzed the crystallization and surface areas of the samples. From XRD patterns in Figure 1 we can see that the peaks are intensifying and sharpening as the hydrothermal temperature rises. That means higher synthetic temperatures bring about better crystallinity. The crystallization order is ZS-230 > ZS-200 > ZS-180 > ZS-140. However, it does not go along with the order of photocatalytic activities, indicating the crystallization does not contribute directly to their H_2 production. Then we evaluated the specific surface area of each sample by BET methods (Supporting Information, Table S2). The surface areas are sorted by ZS-180 > ZS-200 > ZS-230 > ZS-140, and that of w-ZS-E (86.62 m2g-1) fabricated in ethanol solvent is more than twice these, which does not fit the trend of H_2 evolution performances either. On the contrary, it is easy to realize that the trend of H_2 evolution is similar to the density sequence of sulfur vacancies (Figure 4b). Moreover, when excluding the contribution of BET surface areas, the
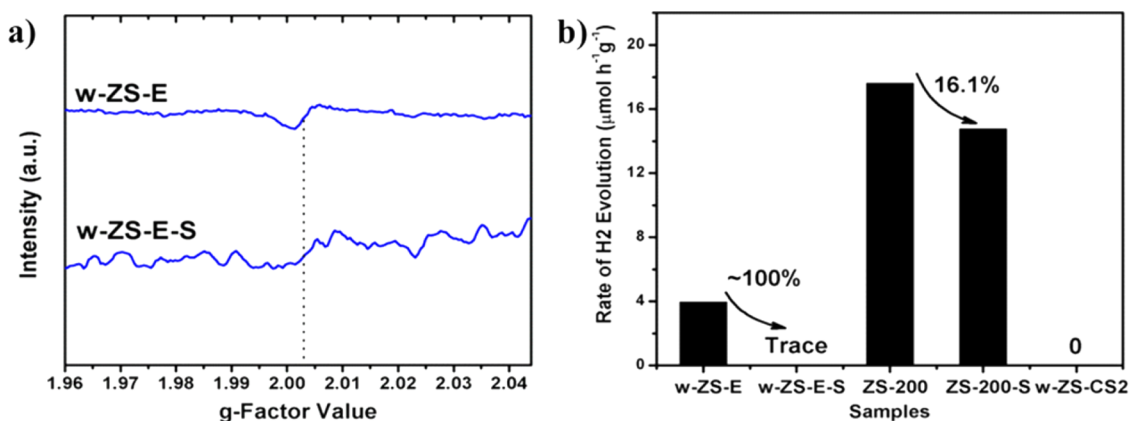

Figure 8. (a) Room-temperature ESR lines of the pristine w-ZS-E and the sulfur-repaired w-ZS-E (w-ZS-E-S); (b) Compared photocatalytic HER performances of different samples under visible-light irradiation ($\lambda \geq 410$ nm).

normalized rates of H_2 evolution per surface area (Figure 7, black bars) match well with the density sequence of sulfur vacancies. The results demonstrate the sulfur vacancies-determined visible-light photocatalysis of our defective ZnS systems.

Besides, as to our defective mixed-phase ZnS systems, the H_2 production of ZS-200 apparently decreases when recycled. The activity in the third run only reaches ca. two-thirds of the first run (Supporting Information, Figure S6). Further studies on the deactivation mechanism and corresponding strategy are still needed to improve the activity and stability for practical applications.

The Necessity of Sulfur Vacancies and S−W Phase Junctions. To reveal the further relationship between the photocatalytic HER activities and the constructed defective mixed-phase structures in the catalysts, we investigated the necessity of sulfur vacancies and S−W phase junctions to the photocatalytic performance, respectively. To restore the sulfur vacancy sites, excess S powder was used to react with the as-prepared samples (details in Supporting Information). After such a process, sulfur vacancies in w-ZS-E, for example, can be reduced as the ESR signal of sulfur vacancies decreases (Figure 8a). The sulfurized w-ZS-E (donated as w-ZS-E-S) keeps the same crystalline structure as w-ZS-E while losing the photocatalytic ability (Figure 8b). A cut-down activity is also observed for the treated ZS-200, that is, ZS-200-S, which keeps the same XRD patterns as well. The comparison of these results establishes the essentiality of sulfur vacancies for the present visible-light-driven performances. In terms of the necessity of the S−W phase junctions, the photoactivity of single-phase wurtzite ZnS sample with sulfur vacancies was monitored in the same condition. The strong well-indexed XRD peaks (Supporting Information, Figure S1) demonstrate the good crystallinity and high purity of wurtzite ZnS, suggesting the absence of S−W phase junctions. ESR experiments show an obvious signal located at $g = 2.003$ (Supporting Information, Figure S7), implying the existence of sulfur vacancies. No H_2 was detected after 4 h of visible-light irradiation in the HER activity test (Figure 8b). Thus, these results credibly support the necessity of S−W phase junctions in ZnS to work in the visible-light-driven reaction.

Charge Behaviors and the Mechanism in the Mixed-Phase Defective ZnS Systems. Since sulfur vacancies are located in the nascent wurtzite phase beside the junctions, defect energy levels should be formed in the band gap of wurtzite rather than sphalerite. And owing to the nature to attract electrons of sulfur vacancies, corresponding energy levels should be identified as acceptor levels, that is, electrons in VB of wurtzite are supposed to be excited up to energy levels of sulfur vacancies under visible-light irradiation. The subsequent photoexciton behaviors including transfer and recombination determine the efficiency of photocatalytic reactions, in which the constructed type II S−W phase junction performs its functions. Herein, the photoluminescence (PL) experiment was employed to estimate the photoexciton behaviors[65] under a visible-light excitation at 420 nm (Figure 9). After photoexcitation, there are always parts of the electrons that transfer belatedly in the sulfur vacancy levels and tend to recombine with the holes in VB of wurtzite, inducing a photon emission (donated as Emission **I**). Meanwhile, the type II phase junctions can drive the holes in the VB of wurtzite to the VB of sphalerite through the junction channel by the potential difference. Thus, electrons in sulfur vacancy levels become free
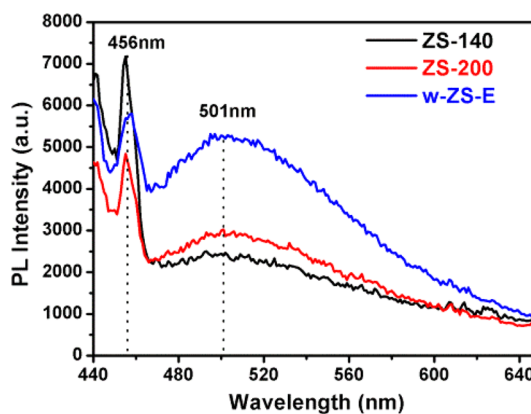

Figure 9. Photoluminescence spectra (PL) of ZnS samples excited at 420 nm.

electrons to react with H^+ at the spatial sulfur vacancy site, whereas some of them can transit down to recombine with the transferred holes in the VB of sphalerite through the in situ junction channel with ohmic contact,[66] emitting photons with lower energy (donated as Emission **II**) than Emission **I**. Therefore, two sorts of emission peaks can be obtained at different wavelengths. As shown in Figure 9, two emission peaks are located at 456 nm (photon energy: 2.72 eV) and 501 nm (photon energy: 2.48 eV), respectively. The photon energy difference of the two emission peaks is consistent with the difference between the VB potentials (0.23 eV) of sphalerite and wurtzite. Thereby, it is reasonable to assign PL peaks at 456 and 501 nm to Emission **I** and Emission **II**, respectively.

The peaks at 456 nm with the intensity order of ZS-140 > w-ZS-E > ZS-200 suggest the recombination degrees via Emission **I** in the samples follow the same order. Likewise, the recombination extents via Emission **II** are w-ZS-E > ZS-200 > ZS-140 according to the PL intensities at 501 nm. For ZS-140, the introduced trace sulfur vacancies enable ZS-140 to generate limited amount of photoexcitons, but the insufficient S−W phase junctions fail to drive an apparent exciton separation so that ZS-140 shows the strongest PL peak at 456 nm and the weakest at 501 nm, leading a trace activity. Compared with ZS-140, the enhanced sulfur vacancies make w-ZS-E to better respond to the visible light and the residual phase junctions contribute to the transfer of holes, inducing the relatively low peak at 456 nm. The strongest emission peak at 501 nm implies that most of the electrons are consumed in the recombination via Emission **II**, which reveals the reason for the low activity. As to ZS-200, which possesses a balanced amount of S−W phase junctions, an excellent exciton separation proved by the lowest PL peak at 456 nm can be achieved to capacitate the generation of free electrons. Compared with w-ZS-E, the much lower PL peak of ZS-200 at 501 nm demonstrates that free electrons in ZS-200 can be effectively utilized in the reactions rather than the recombination with the transferred holes, inducing the best performance in the photocatalytic HER. Therefore, the mechanism for the visible-light-driven HER activities is comprehended (Figure 10).

■ CONCLUSIONS

In summary, defective ZnS systems with sphalerite−wurtzite phase junctions are constructed by the temperature-dependent phase transformation through hydrothermal and solvothermal treatments. The formation mechanism of the symbiotic sulfur
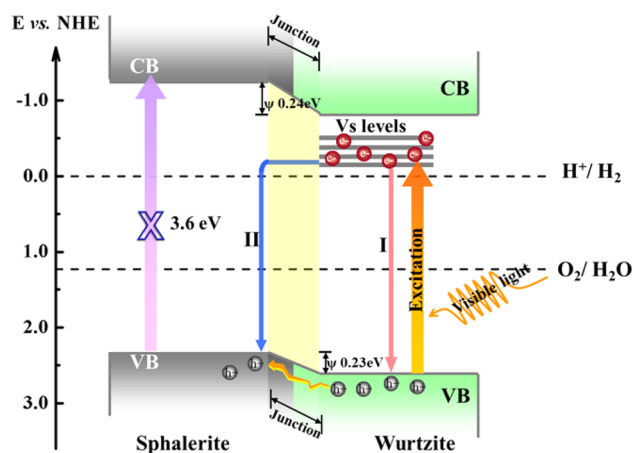
Figure 10. Proposed mechanism for defective ZnS with S—W phase junction under visible-light excitation (Vs is short for sulfur vacancy).

vacancies and phase junctions are discussed. The density of sulfur vacancies is regulated by the extent of phase transformation. Dual roles of the sulfur vacancies in wurtzite phase of ZnS are reported, serving as photosensitization units that induce visible light response and as active sites that trap electrons for proton reduction. The sphalerite—wurtzite phase junction with a type II band structure dominates the charge transfer kinetics for the significant photoexciton separation. When amount-balanced sulfur vacancies and phase junctions cooperate with each other, the desirable visible-light-driven activities in H_2 evolution for the wide-bandgap ZnS are achieved. The present strategy of intrinsic modification on ZnS will not only contribute to the realization of visible-light photocatalysis for wide-bandgap semiconductors but also broaden our vision of the design for highly efficient transition metal sulfide photocatalysts.

ASSOCIATED CONTENT

Ⓢ Supporting Information
Details of syntheses, tabulated data indicating intensity ratio of XRD peaks, XRD patterns, TEM and HRTEM images, Nyquist impedence plots, room-temperature ESR spectra, UV-vis diffuse reflectance spectra, plot of transformed Kubelka—Munk function versus the energy of the excitation source absorbed, tabulated data indicating measured surface area, cycle runs for the photocatalytic H_2 production, bar graph indicating calculated rate of H_2 production, and potential versus NHE comparison of energy levels in defective wurtzite. The Supporting Information is available free of charge on the ACS Publications website at DOI: 10.1021/acsami.5b02641.

AUTHOR INFORMATION

Corresponding Authors
*E-mail: liuping@fzu.edu.cn. (L.P.)
*E-mail: slin@fzu.edu.cn. (S.L.)
*E-mail: xzfu@fzu.edu.cn. (X.F.)
Notes
The authors declare no competing financial interest.

ACKNOWLEDGMENTS

REFERENCES

(1) Khan, S. U.; Al-Shahry, M.; Ingler, W. B., Jr. Efficient photochemical water splitting by a chemically modified n-TiO$_2$. *Science* **2002**, *297* (5590), 2243–5.

(2) Han, Z.; Qiu, F.; Eisenberg, R.; Holland, P. L.; Krauss, T. D. Robust photogeneration of H_2 in water using semiconductor nanocrystals and a nickel catalyst. *Science* **2012**, *338* (6112), 1321–4.

(3) Zhou, H.; Qu, Y.; Zeid, T.; Duan, X. Towards highly efficient photocatalysts using semiconductor nanoarchitectures. *Energy Environ. Sci.* **2012**, *5* (5), 6732.

(4) Hong, Y.; Zhang, J.; Wang, X.; Wang, Y.; Lin, Z.; Yu, J.; Huang, F. Influence of lattice integrity and phase composition on the photocatalytic hydrogen production efficiency of ZnS nanomaterials. *Nanoscale* **2012**, *4* (9), 2859–62.

(5) Reber, J. F.; Meier, K. Photochemical production of hydrogen with zinc sulfide suspensions. *J. Phys. Chem.* **1984**, *88* (24), 5903–5913.

(6) Tsuji, I.; Kato, H.; Kudo, A. Photocatalytic Hydrogen Evolution on ZnS—CuInS$_2$—AgInS$_2$ Solid Solution Photocatalysts with Wide Visible Light Absorption Bands. *Chem. Mater.* **2006**, *18* (7), 1969–1975.

(7) Chen, X.; Liu, L.; Yu, P. Y.; Mao, S. S. Increasing solar absorption for photocatalysis with black hydrogenated titanium dioxide nanocrystals. *Science* **2011**, *331* (6018), 746–50.

(8) Zhou, C.; Ma, Z.; Ren, Z.; Mao, X.; Dai, D.; Yang, X. Effect of defects on photocatalytic dissociation of methanol on TiO$_2$(110). *Chem. Sci.* **2011**, *2* (10), 1980.

(9) Kong, M.; Li, Y.; Chen, X.; Tian, T.; Fang, P.; Zheng, F.; Zhao, X. Tuning the relative concentration ratio of bulk defects to surface defects in TiO$_2$ nanocrystals leads to high photocatalytic efficiency. *J. Am. Chem. Soc.* **2011**, *133* (41), 16414–7.

(10) Long, R.; English, N. J.; Prezhdo, O. V. Defects are needed for fast photo-induced electron transfer from a nanocrystal to a molecule: time-domain ab initio analysis. *J. Am. Chem. Soc.* **2013**, *135* (50), 18892–900.

(11) Pei, Z.; Ding, L.; Lin, H.; Weng, S.; Zheng, Z.; Hou, Y.; Liu, P. Facile synthesis of defect-mediated TiO$_{2-x}$ with enhanced visible light photocatalytic activity. *J. Mater. Chem. A* **2013**, *1* (35), 10099.

(12) Zhang, J.; Xu, Q.; Feng, Z.; Li, M.; Li, C. Importance of the relationship between surface phases and photocatalytic activity of TiO$_2$. *Angew. Chem.* **2008**, *47* (9), 1766–9.

(13) Wang, X.; Xu, Q.; Li, M.; Shen, S.; Wang, X.; Wang, Y.; Feng, Z.; Shi, J.; Han, H.; Li, C. Photocatalytic overall water splitting promoted by an alpha-beta phase junction on Ga$_2$O$_3$. *Angew. Chem.* **2012**, *51* (52), 13089–92.

(14) Zhou, C.; Ren, Z.; Tan, S.; Ma, Z.; Mao, X.; Dai, D.; Fan, H.; Yang, X.; LaRue, J.; Cooper, R.; Wodtke, A. M.; Wang, Z.; Li, Z.; Wang, B.; Yang, J.; Hou, J. Site-specific photocatalytic splitting of methanol on TiO$_2$(110). *Chem. Sci.* **2010**, *1* (5), 575.

(15) Yu, J.; Low, J.; Xiao, W.; Zhou, P.; Jaroniec, M. Enhanced Photocatalytic CO$_2$-Reduction Activity of Anatase TiO$_2$ by Coexposed {001} and {101} Facets. *J. Am. Chem. Soc.* **2014**, *136* (25), 8839–8842.

(16) Liu, S.; Wang, X.; Wang, K.; Lv, R.; Xu, Y. ZnO/ZnS—PdS core/shell nanorods: Synthesis, characterization and application for photocatalytic hydrogen production from a glycerol/water solution. *Appl. Surf. Sci.* **2013**, *283*, 732–739.

(17) Kudo, A.; Sekizawa, M. Photocatalytic H_2 evolution under visible light irradiation on Ni-doped ZnS photocatalyst. *Chem. Commun.* **2000**, *15*, 1371–1372.

(18) Zhang, J.; Liu, S.; Yu, J.; Jaroniec, M. A simple cation exchange approach to Bi-doped ZnS hollow spheres with enhanced UV and visible-light photocatalytic H$_2$-production activity. *J. Mater. Chem.* **2011**, *21* (38), 14655.

(19) Yu, Y.; Chen, G.; Wang, Q.; Li, Y. Hierarchical architectures of porous ZnS-based microspheres by assembly of heterostructure

nanoflakes: lateral oriented attachment mechanism and enhanced photocatalytic activity. *Energy Environ. Sci.* **2011**, *4* (9), 3652.

(20) Zhang, J.; Wang, Y.; Zhang, J.; Lin, Z.; Huang, F.; Yu, J. Enhanced photocatalytic hydrogen production activities of Au-loaded ZnS flowers. *ACS Appl. Mater. Interfaces* **2013**, *5* (3), 1031−7.

(21) Zhang, J.; Yu, J.; Zhang, Y.; Li, Q.; Gong, J. R. Visible light photocatalytic H(2)-production activity of CuS/ZnS porous nanosheets based on photoinduced interfacial charge transfer. *Nano Lett.* **2011**, *11* (11), 4774−9.

(22) Wang, D. H.; Wang, L.; Xu, A. W. Room-temperature synthesis of $Zn_{(0.80)}Cd_{(0.20)}S$ solid solution with a high visible-light photocatalytic activity for hydrogen evolution. *Nanoscale* **2012**, *4* (6), 2046−53.

(23) Zou, Y.; Su, X.; Jiang, J. Phase-controlled synthesis of Cu_2ZnSnS_4 nanocrystals: the role of reactivity between Zn and S. *J. Am. Chem. Soc.* **2013**, *135* (49), 18377−84.

(24) Liu, M.; Wang, L.; Lu, G.; Yao, X.; Guo, L. Twins in $Cd_{1−x}Zn_xS$ solid solution: Highly efficient photocatalyst for hydrogen generation from water. *Energy Environ. Sci.* **2011**, *4* (4), 1372.

(25) Huang, L.; Wang, X.; Yang, J.; Liu, G.; Han, J.; Li, C. Dual Cocatalysts Loaded Type I CdS/ZnS Core/Shell Nanocrystals as Effective and Stable Photocatalysts for H_2 Evolution. *J. Phys. Chem. C* **2013**, *117* (22), 11584−11591.

(26) Lei, Z.; You, W.; Liu, M.; Zhou, G.; Takata, T.; Hara, M.; Domen, K.; Li, C. Photocatalytic water reduction under visible light on a novel $ZnIn_2S_4$ catalyst synthesized by hydrothermal method. *Chem. Commun.* **2003**, *17*, 2142.

(27) Soltani, N.; Saion, E.; Yunus, W. M. M.; Erfani, M.; Navasery, M.; Bahmanrokh, G.; Rezaee, K. Enhancement of visible light photocatalytic activity of ZnS and CdS nanoparticles based on organic and inorganic coating. *Appl. Surf. Sci.* **2014**, *290*, 440−447.

(28) Qadri, S.; Skelton, E.; Hsu, D.; Dinsmore, A.; Yang, J.; Gray, H.; Ratna, B. Size-induced transition-temperature reduction in nanoparticles of ZnS. *Phys. Rev. B* **1999**, *60* (13), 9191−9193.

(29) Jiang, Y.; Meng, X. M.; Liu, J.; Xie, Z. Y.; Lee, C. S.; Lee, S. T. Hydrogen-Assisted Thermal Evaporation Synthesis of ZnS Nanoribbons on a Large Scale. *Adv. Mater.* **2003**, *15* (4), 323−327.

(30) Zhou, G.-T.; Wang, X.; Yu, J. C. A Low-Temperature and Mild Solvothermal Route to the Synthesis of Wurtzite-Type ZnS With Single-Crystalline Nanoplate-like Morphology. *Cryst. Growth Des.* **2005**, *5* (5), 1761−1765.

(31) Yu, S. H.; Yoshimura, M. Shape and Phase Control of ZnS Nanocrystals: Template Fabrication of Wurtzite ZnS Single-Crystal Nanosheets and ZnO Flake-like Dendrites from a Lamellar Molecular Precursor ZnS·$(NH_2CH_2CH_2NH_2)_{0.5}$. *Adv. Mater.* **2002**, *14* (4), 296−300.

(32) Deng, Z.-X.; Wang, C.; Sun, X.-M.; Li, Y.-D. Structure-Directing Coordination Template Effect of Ethylenediamine in Formations of ZnS and ZnSe Nanocrystallites via Solvothermal Route. *Inorg. Chem.* **2002**, *41* (4), 869−873.

(33) Watkins, G. D. Intrinsic defects in II−VI semiconductors. *J. Cryst. Growth* **1996**, *159* (1−4), 338−344.

(34) Bear, J. C.; Hollingsworth, N.; McNaughter, P. D.; Mayes, A. G.; Ward, M. B.; Nann, T.; Hogarth, G.; Parkin, I. P. Copper-doped CdSe/ZnS quantum dots: controllable photoactivated copper(I) cation storage and release vectors for catalysis. *Angew. Chem.* **2014**, *53* (6), 1598−601.

(35) Chen, R.; Li, D.; Liu, B.; Peng, Z.; Gurzadyan, G. G.; Xiong, Q.; Sun, H. Optical and excitonic properties of crystalline ZnS nanowires: toward efficient ultraviolet emission at room temperature. *Nano Lett.* **2010**, *10* (12), 4956−61.

(36) Xiong, Q.; Chen, G.; Acord, J. D.; Liu, X.; Zengel, J. J.; Gutierrez, H. R.; Redwing, J. M.; Lew Yan Voon, L. C.; Lassen, B.; Eklund, P. C. Optical Properties of Rectangular Cross-sectional ZnS Nanowires. *Nano Lett.* **2004**, *4* (9), 1663−1668.

(37) Wang, Y.; Liang, X.; Ma, X.; Hu, Y.; Hu, X.; Li, X.; Fan, J. Simple and greener synthesis of highly photoluminescence Mn^{2+}-doped ZnS quantum dots and its surface passivation mechanism. *Appl. Surf. Sci.* **2014**, *316*, 54−61.

(38) Hou, J.; Yang, C.; Wang, Z.; Zhou, W.; Jiao, S.; Zhu, H. In situ synthesis of $\alpha−\beta$ phase heterojunction on Bi_2O_3 nanowires with exceptional visible-light photocatalytic performance. *Appl. Cat., B* **2013**, *142−143*, 504−511.

(39) Acharya, S. A.; Maheshwari, N.; Tatikondewar, L.; Kshirsagar, A.; Kulkarni, S. K. Ethylenediamine-Mediated Wurtzite Phase Formation in ZnS. *Cryst. Growth Des.* **2013**, *13* (4), 1369−1376.

(40) Kresse, G.; Furthmüller, J. Efficiency of ab initio total energy calculations for metals and semiconductors using a plane-wave basis set. *Comput. Mater. Sci.* **1996**, *6* (1), 15−50.

(41) Kresse, G. Efficient iterative schemes for ab initio total-energy calculations using a plane-wave basis set. *Phys. Rev. B* **1996**, *54* (16), 11169−11186.

(42) Kresse, G.; Hafner, J. Ab initio molecular dynamics for liquid metals. *Phys. Rev. B* **1993**, *47* (1), 558−561.

(43) Perdew, J. P.; Jackson, K. A.; Pederson, M. R.; Singh, D. J.; Fiolhais, C. Atoms, molecules, solids, and surfaces: Applications of the generalized gradient approximation for exchange and correlation. *Phys. Rev. B* **1992**, *46* (11), 6671−6687.

(44) Blöchl, P. E. Projector augmented-wave method. *Phys. Rev. B* **1994**, *50* (24), 17953−17979.

(45) Kresse, G.; Joubert, D. From ultrasoft pseudopotentials to the projector augmented-wave method. *Phys. Rev. B* **1999**, *59* (3), 1758−1775.

(46) Monkhorst, H. J.; Pack, J. D. Special points for Brillouin-zone integrations. *Phys. Rev. B* **1976**, *13* (12), 5188−5192.

(47) Huang, F.; Zhang, H.; Banfield, J. F. Two-Stage Crystal-Growth Kinetics Observed during Hydrothermal Coarsening of Nanocrystalline ZnS. *Nano Lett.* **2003**, *3* (3), 373−378.

(48) Huang, F.; Banfield, J. F. Size-dependent phase transformation kinetics in nanocrystalline ZnS. *J. Am. Chem. Soc.* **2005**, *127* (12), 4523−9.

(49) Milliron, D. J.; Hughes, S. M.; Cui, Y.; Manna, L.; Li, J.; Wang, L. W.; Alivisatos, A. P. Colloidal nanocrystal heterostructures with linear and branched topology. *Nature* **2004**, *430* (6996), 190−5.

(50) Wang, D.; Choi, D.; Li, J.; Yang, Z.; Nie, Z.; Kou, R.; Hu, D.; Wang, C.; Saraf, L. V.; Zhang, J.; Aksay, I. A.; Liu, J. Self-assembled TiO_2-graphene hybrid nanostructures for enhanced Li-ion insertion. *ACS Nano* **2009**, *3* (4), 907−14.

(51) Yan, K.; Zhang, L.; Qiu, J.; Qiu, Y.; Zhu, Z.; Wang, J.; Yang, S. A Quasi-Quantum Well Sensitized Solar Cell with Accelerated Charge Separation and Collection. *J. Am. Chem. Soc.* **2013**, *135* (25), 9531−9539.

(52) Gonzalez Beermann, P. A.; McGarvey, B. R.; Muralidharan, S.; Sung, R. C. W. EPR Spectra of Mn^{2+}-Doped ZnS Quantum Dots. *Chem. Mater.* **2004**, *16* (5), 915−918.

(53) Nistor, S. V.; Stefan, M. In-depth investigation of EPR spectra of Mn(2+) ions in ZnS single crystals with pure cubic structure. *J. Phys.: Condens. Matter* **2009**, *21* (14), 145408.

(54) Tetsuya Arizumi, T. M. Koichi Shimakawa, EPR Study on Surface Properties of ZnS and CdS. *Jpn. J. Appl. Phys.* **1969**, *8* (12), 1411−1416.

(55) Shono, Y. Electron Spin Resonance Study of Electron-Irradiated ZnS Crystals Containing Stacking Faults. *J. Phys. Soc. Jpn.* **1979**, *47* (2), 590−598.

(56) Leutwein, K.; Räuber, A.; Schneider, J. Optical and photoelectric properties of the F-centre in ZnS. *Solid State Commun.* **1967**, *5* (9), 783−786.

(57) Shono, Y.; Oka, T. Complex defects in electron-irradiated ZnS. *J. Cryst. Growth* **2000**, *210* (1−3), 278−282.

(58) Brunner, S.; Puff, W.; Balogh, A. G.; Mascher, P. Induced defects in ZnS by electron and proton irradiation and defect-annealing behavior. *Phys. B: Condens. Matter* **1999**, *273−274*, 898−901.

(59) Dersch, H.; Schweitzer, L.; Stuke, J. Recombination processes in α-Si:H: Spin-dependent photoconductivity. *Phys. Rev. B* **1983**, *28* (8), 4678−4684.

(60) Godefroo, S.; Hayne, M.; Jivanescu, M.; Stesmans, A.; Zacharias, M.; Lebedev, O. I.; Van Tendeloo, G.; Moshchalkov, V. V.

Classification and control of the origin of photoluminescence from Si nanocrystals. *Nature Nanotechnol.* **2008**, *3* (3), 174−8.

(61) Liu, G.; Niu, P.; Yin, L.; Cheng, H. M. alpha-Sulfur crystals as a visible-light-active photocatalyst. *J. Am. Chem. Soc.* **2012**, *134* (22), 9070−3.

(62) Yaghoubi, H.; Li, Z.; Chen, Y.; Ngo, H. T.; Bhethanabotla, V. R.; Joseph, B.; Ma, S.; Schlaf, R.; Takshi, A. Toward a Visible Light-Driven Photocatalyst: The Effect of Midgap-States-Induced Energy Gap of Undoped TiO_2 Nanoparticles. *ACS Catal.* **2015**, *5* (1), 327−335.

(63) Takata, T.; Domen, K. Defect Engineering of Photocatalysts by Doping of Aliovalent Metal Cations for Efficient Water Splitting. *J. Phys. Chem. C* **2009**, *113* (45), 19386−19388.

(64) Maeda, K.; Teramura, K.; Domen, K. Effect of post-calcination on photocatalytic activity of $(Ga_{1-x}Zn_x)(N_{1-x}O_x)$ solid solution for overall water splitting under visible light. *J. Catal.* **2008**, *254* (2), 198−204.

(65) Lee, J.-C.; Park, D.-H. Self-defects properties of ZnS with sintering temperature. *Mater. Lett.* **2003**, *57* (19), 2872−2878.

(66) Zhou, P.; Yu, J.; Jaroniec, M. All-solid-state Z-scheme photocatalytic systems. *Adv. Mater.* **2014**, *26* (29), 4920−35.